Earth and Planetary Science Letters 524 (2019) 115721

Contents lists available at ScienceDirect

Earth and Planetary Science Letters

www.elsevier.com/locate/epsl

Constraints on the volume and rate of Deccan Traps flood basalt eruptions using a combination of high-resolution terrestrial mercury records and geochemical box models

Isabel M. Fendley [a,*], Tushar Mittal [a], Courtney J. Sprain [b], Mark Marvin-DiPasquale [c], Thomas S. Tobin [d], Paul R. Renne [a,e]

[a] University of California Berkeley, Department of Earth and Planetary Science, 307 McCone Hall, Berkeley, CA, 94720, USA
[b] Department of Earth, Ocean and Ecological Sciences, University of Liverpool, Liverpool, L69 3GP, United Kingdom
[c] US Geological Survey, 345 Middlefield Road, Menlo Park, CA 94025, USA
[d] University of Alabama, Department of Geological Sciences, Box 870338, Tuscaloosa, AL, 35476, USA
[e] Berkeley Geochronology Center, 2455 Ridge Rd Berkeley, CA, 94709, USA

ARTICLE INFO

Article history:
Received 24 February 2019
Received in revised form 18 July 2019
Accepted 19 July 2019
Available online xxxx
Editor: T.A. Mather

Keywords:
mass extinction
mercury
volcanism
chemostratigraphy
Deccan Traps
Large Igneous Province

ABSTRACT

Deccan Traps continental flood basalt eruptions spanned the Cretaceous-Paleogene mass extinction, erupting over a million cubic kilometers of basalt over a total duration of approximately a million years. The environmental consequences of flood basalt eruptions depend on the timing and amount of volatile release; eruption rates are thus needed to evaluate their potential to cause climate change. Radioisotopic dates are not currently sufficient to resolve sub-ten thousand year eruptive tempos, necessary for constraining the effects of short-lifetime volatiles including sulfur dioxide. Recent studies have demonstrated that increases in mercury concentration in sedimentary records correlate with flood basalt eruptions under some circumstances. However, mercury concentrations have primarily been used to show the presence or absence of flood basalt eruptions. We show that this proxy can be used to quantitatively estimate eruptive rates using a mercury geochemical cycle framework. We illustrate this using new mercury chemostratigraphic records from terrestrial Cretaceous-Paleogene boundary sections in eastern Montana, USA, with multiple high-resolution chronologic constraints. We estimate that Deccan eruptions lasted on the order of centuries and released 500–3000 megagrams (Mg) of mercury per year, corresponding to ∼50–250 km^3/a of lava. The box model framework highlights the importance of carefully accounting for differences in sedimentation rate and sampling resolution when comparing mercury records from different locations and depositional environments. While there are uncertainties in the box model estimates due to possible variation in flood basalt mercury emissions and sedimentation rates, they provide a useful framework to quantitatively evaluate the global mercury budget change indicated by changing concentration in sedimentary records. Eruptions of the estimated size would have released enough SO_2, if it reached the stratosphere, to cause significant cooling for the duration of the eruption. However, given our constraints on the duration of individual eruptions, these colder periods are likely too brief to be clearly visible in most existing paleoclimate records.

1. Introduction

The end of the Cretaceous Period was a time of profound environmental change, which culminated in the extinction of all non-avian dinosaurs among many other organisms (e.g. Schulte et al., 2010). Two catastrophic events were coeval with the extinction – the Chicxulub bolide impact and Deccan Traps continental flood basalt eruptions (e.g. Renne et al., 2013). Both the impact and the Deccan eruptions had the potential to cause global climate change, releasing thousands of Tg of climatically active gases such as sulfur dioxide (SO_2, leads to sulfate aerosol driven cooling) and carbon dioxide (CO_2, greenhouse warming) (e.g. Self et al., 2006).

The climate effects of these gases occur on different timescales and are directly related to the eruptive flux, neglecting the contributions of volatiles emitted during quiescent intervals (e.g. Black et al., 2018; Self et al., 2014). Deccan eruptive events are hypothesized to have emitted enough SO_2 to cause significant and rapid global cooling, whereby the duration of the cold interval is

* Corresponding author.
E-mail address: isabel.fendley@berkeley.edu (I.M. Fendley).

https://doi.org/10.1016/j.epsl.2019.115721
0012-821X/

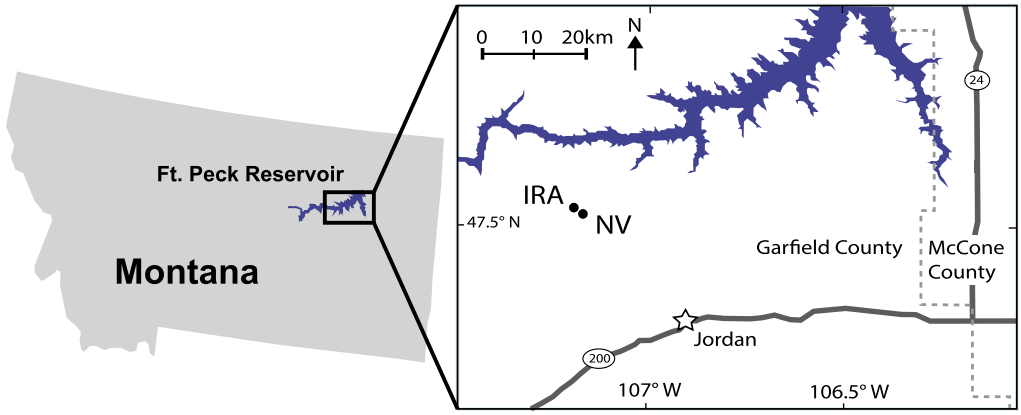

Fig. 1. Map of the studied localities in eastern Montana, USA. The star indicates the town of Jordan, MT. The Nirvana locality is labeled as NV; Iridium Hill Annex is labeled as IRA.

proportional to the duration of the eruption, as SO_2's lifetime in the atmosphere is short: weeks in the troposphere, a few years in the stratosphere (e.g. Schmidt et al., 2016). In contrast, carbon cycle models indicate that CO_2 pulses persist for thousands of years in the atmosphere (e.g. Zeebe, 2012). Consequently, CO_2 may accumulate through multiple eruptive events and lead to greenhouse warming on longer timescales (e.g. Archer et al., 2009; Self et al., 2006; Tobin et al., 2016). The extent of these climate effects depends on both the quantity and rate at which volcanogenic CO_2 and SO_2 is released, as well as the length of hiatuses between eruptions (e.g. Black et al., 2018). Therefore in order to determine the climatic effects of Deccan volcanism, it is necessary to understand the eruptive rate at a resolution comparable to individual eruptions (Self et al., 2014).

While the main Deccan eruptive sequence lasted for approximately a million years, active eruptions potentially occurred only a few percent of the time (e.g. Self et al., 2014). Dates of Deccan basalts place the Cretaceous-Paleogene boundary near the beginning of the most voluminous eruptive interval, the Wai subgroup (Schoene et al., 2019; Sprain et al., 2019). The current maximum level of precision for any radioisotopic dating technique on Cretaceous-age basalt is tens of thousands of years; however, individual eruptive events for flood basalts have been hypothesized to be ten to hundreds of years in duration based on physical and petrologic properties of lava flows (Self et al., 2006; Thordarson and Self, 1996). Consequently, while radioisotopic dates are an essential tool in determining cumulative eruptive rates throughout the entire Deccan sequence, they cannot presently provide sub-ten thousand year eruptive records as required.

Mercury is used as a tracer of flood basalt eruptions, as volcanogenic mercury is deposited into sediments geologically rapidly (Percival et al., 2015; Sanei et al., 2012). Volcanism is a major natural source of mercury to the environment, and it is recycled through different environmental reservoirs (e.g. Fitzgerald and Lamborg, 2014 and references therein). The residence time for gaseous mercury is ~9 months in the atmosphere, which is long enough to be distributed globally, though not necessarily homogeneously (Chen et al., 2018). Atmospheric mercury gas can be oxidized, dissolved into water vapor and rained out, or directly taken up by biota. Aqueous or biotic mercury on continents frequently accumulates in rivers and lakes, and a significant fraction is adsorbed onto sediment or particulate material (e.g. Driscoll et al., 2007). Mercury in continental waterways either reaches the ocean or is buried in fluvial or lacustrine sediment. In sediment, the mercury may be associated with organic carbon or sulfur, and it is important to consider interactions with these species. Models indicate that although the time between the emission of gaseous mercury and final burial in sediment ranges from almost immediate to several thousand years, the majority is buried within a thousand years (Amos et al., 2014).

The abundance of sedimentary mercury has previously been used as an indicator of Deccan volcanic eruptions (e.g. Font et al., 2016; Sial et al., 2016; Keller et al., 2018; Percival et al., 2018). However, the interpretation has focused primarily on the presence or absence of mercury concentration peaks at a particular time interval. Most records display increases in mercury concentration in the vicinity of the Cretaceous-Paleogene boundary, indicating a potential increase of the global mercury budget. Comparison of these records from multiple locations indicates variation in peak sizes and timing, possibly due to uncertainty in chronology, sediment accumulation rate (SAR), and lithologic changes (Percival et al., 2018). Well-characterized environmental mercury box models present an opportunity to investigate and compare these records quantitatively, and to estimate the eruptive flux required to produce a mercury concentration peak. Herein we present a high-resolution terrestrial mercury record with precise chronologic constraints to improve understanding of volcanism around the Cretaceous-Paleogene boundary. Then, we describe a model framework for assessing global mercury cycle change indicated by a concentration change in sedimentary records.

2. Geologic setting

This study examines the mercury record around the Cretaceous-Paleogene boundary from two terrestrial sites, Iridium Hill Annex and Nirvana, within the Cretaceous Hell Creek Formation and the Paleogene Tullock Member of the Fort Union Formation in northeastern Montana (Fig. 1). These units are composed of fluvial and floodplain deposits, mainly claystones to siltstones, with occasional crossbedded sandstones and lignite seams within the more finely bedded Tullock Member. Rivers transport mercury from continental biomass and sediments to the ocean, dominantly as particulate mercury species (Amos et al., 2014; Cossa et al., 1996). Fluvial sediments are therefore likely to increase in mercury concentration following an increase in mercury within proximal soils or biomass. This conclusion is corroborated by an increase in mercury concentrations in modern fluvial sediments due to anthropogenic mercury release (e.g. Amos et al., 2014; Fitzgerald and Lamborg, 2014 and references therein).

The Hell Creek and Fort Union formations have been extensively studied, and a detailed chronostratigraphy has been established based on radioisotopically dated volcanic tephra layers and magnetostratigraphy (Fastovsky and Bercovici, 2016 and references therein; Sprain et al., 2018, 2015). The Cretaceous-Paleogene boundary is recognized here by an impact ejecta claystone and iridium anomaly within the "Iridium Z" coal seam (Alvarez, 1983),

and a tephra layer within a few centimeters of the claystone has been radioisotopically dated in both sites examined in this study with a pooled date of 66.052 Ma (Renne et al., 2013; Sprain et al., 2018, and references therein).

3. Methods

3.1. Chemical analyses

3.1.1. Sample preparation

Samples were collected from trenches exposing visibly unweathered rock, wrapped in aluminum foil and placed into plastic bags. Samples which contained any roots or traces of modern plant/fungal material were not analyzed. Stratigraphic sections were recorded simultaneously with sample collection. Samples were crushed to a fine powder using a ceramic mortar and pestle, then freeze-dried and stored in a desiccator prior to mercury concentration (THg) analysis. An aliquot was retained for organic carbon concentration (TOC) analysis.

3.1.2. THg analysis

All analyses were performed at the USGS in Menlo Park following standard methods for solid phase samples (Olund et al., 2004). Samples were initially digested at room temperature with aqua regia (3:1, concentrated $HCl:HNO_3$), then further oxidized by adding 5% bromium monochloride and heated in an oven at 50 °C overnight. Samples were then analyzed with an automated Total Mercury analyzer (Tekran, Model 2600) with cold vapor atomic fluorescence spectrophotometric (CVAFS) detection. Analytical duplicates of homogenized samples yielded a mean (± standard error) percent deviation of 2.6% ± 0.6% ($N = 12$) (Duplicates sheet). Certified reference material (PACS-3, marine sediment, certified value 3.0 μg/g) recoveries were 95.3 ± 2.5% (mean ± standard error, $N = 11$).

3.1.3. TOC analysis

Carbonate was removed from a 70 mg sample aliquot through acidification for 24 h using 3 mL 1 M HCl (e.g. Arens et al., 2014). The samples were then rinsed three times with 5 mL MilliQ water, freeze-dried, and packed into tin capsules. They were analyzed for carbon concentration using a CHNOS Elemental Analyzer (Elementar, Hanau, Germany) at the UC Berkeley Center for Stable Isotope Biogeochemistry. The percent calibration was based in the National Institute of Standards and Technology (Gaithersburg, MD, USA) reference materials. The carbon concentrations of two laboratory quality control standards (soil materials with certified low and high organic content from Elemental Microanalysis, Devon, UK) reproduced their accepted values of 1.61% and 9.20% respectively to 3.7 ± 1.4% (mean ± standard error, $N = 7$). Duplicates of samples, acidified separately, had a mean percent deviation of 4.2 ± 1.9% (± standard error, $N = 8$).

3.2. Stratigraphy and age model

The chronologies of Iridium Hill Annex and Nirvana localities (Fig. 1) are both constrained by $^{40}Ar/^{39}Ar$ dating (Sprain et al., 2018 and references therein). The age model for each locality is determined by linearly interpolating between dated coal seams, and the two records are correlated using the Cretaceous-Paleogene boundary. Each locality contains the Cretaceous-Paleogene boundary within the Iridium Z (IrZ) coal and tephra layer (66.052 ± 0.008 Ma, Sprain et al., 2018) and an additional dated horizon: the top of the Iridium Hill Annex section is the Hauso Flats Z (HFZ) coal, which contains two dated tephra layers (65.973 ± 0.020 Ma, Sprain et al., 2015) and Nirvana contains the McGuire Creek Z (MCZ) coal seam and tephra layer (66.024 ± 0.014 Ma, Ickert et al., 2015; Sprain et al., 2018).

Linear interpolation between dates yields mean sediment accumulation rates (SARs) of 25 cm/ka for Iridium Hill Annex and 14.75 cm/ka for Nirvana. Both localities are entirely within magnetochron C29R, and although paleomagnetic sampling has not been done at these sites, the C29R/C29N reversal has been documented ∼15 m higher than the top of the Iridium Hill Annex section at the nearby Hell Hollow locality (Sprain et al., 2018). Utilizing the mean SARs both records have ∼2 ka resolution on average, <1 ka resolution close to the boundary, and combined they span 40 ka pre- and 80 ka post-impact.

Each of the coals used to calculate the SARs are in the Paleogene, in addition to the IrZ coal at the boundary. Given the lack of any other age constraints in these localities, we continue to utilize the same SAR in the Cretaceous portion of the sections. This extrapolation is justified given the average late Maastrichtian age SAR of 19 ± 4 cm/ka in several Hell Creek Formation localities approximately 50 km from IRA and NV, where a tephra layer in the late Maastrichtian is dated in addition to the MCZ (Sprain et al., 2015).

We acknowledge that in a fluvial/floodplain system, the SAR may not be constant. Nevertheless, it is impossible to determine the SAR more accurately in this interval given the current chronostratigraphic constraints. We note that there are no large channels within these sections and no evidence of prolonged hiatuses in sedimentation. Hiatuses may decrease mercury concentrations in the exposed sediment surface due to dissolution into river water or runoff, which in a fluvial system may be greater magnitude than adsorption of dissolved mercury. The mercury concentration would then presumably return to background levels in overlying sediment.

3.3. Mercury box model

3.3.1. Box model parameters

A box model for modern mercury cycling (Fig. 2) was used to predict when gaseous mercury from a subaerial volcanic eruption is ultimately deposited, as well as estimate the size of atmospheric mercury pulse required to create the peaks in our record (Amos et al., 2015, 2014, 2013) (https://github.com/SunderlandLab/gbc-boxmodel). This model approximates the global mercury cycle as an exchange between seven reservoirs: three terrestrial sediment pools (fast, slow, armored), three ocean water pools, and the atmosphere. The model also incorporates coastal and deep marine sediments as sinks. All rate coefficients and initial/steady state reservoir sizes are based on extensive analysis and calibration with detailed models and observations of the modern mercury cycle (Amos et al., 2015). The box model can produce a good agreement with observed anthropogenic mercury increases in terrestrial peats and lake sediments (Amos et al., 2015).

The lack of detailed spatial or climate parameterization make the box model general enough to extrapolate back to the Cretaceous. However, the rate coefficients may not accurately reflect Cretaceous mercury cycle conditions. There are critical differences between late Cretaceous, early Paleogene, and modern environments. The most important factors for the global mercury cycle are potentially the lack of ice caps and permafrost, a generally warmer global climate, and the runoff and ocean circulation changes that may have accompanied the mass extinction. Ice and snowpack are already not explicitly included in the model (Amos et al., 2013). The potential increase in runoff at the Cretaceous-Paleogene boundary, plus rapid temperature fluctuations, may increase the transfer rate from terrestrial sediments to the ocean. However, the amplitude of these effects is presently not well constrained, even for modern global warming scenarios (Lugato et al., 2018). Lastly,

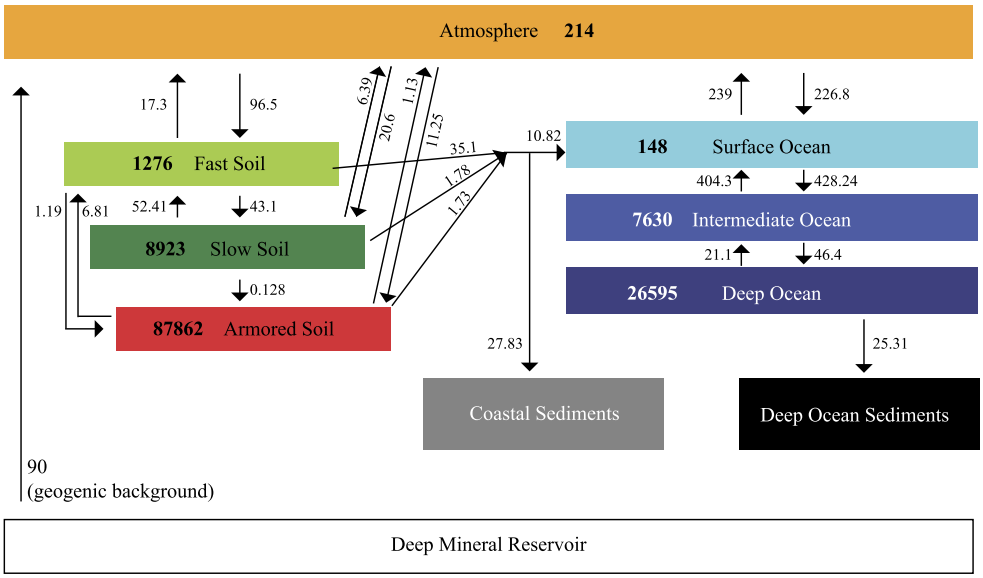

Fig. 2. Schematic for the modern mercury box model utilized in this study (Amos et al., 2013). Steady-state reservoir sizes used are from the most recent model version (Amos et al., 2015) and are reported in Mg and Mg/a respectively. Both reservoir sizes and fluxes will change in response to a perturbation, as fluxes are scaled to the reservoir sizes. Marine sediment and the deep mineral reservoirs do not have steady state sizes, as they are solely sinks and a source respectively. Enrichment factors for marine sediment reservoirs are therefore calculated with respect to the flux. In this model, all input to coastal marine sediment is assumed to be suspended sediment from rivers, deposited on the continental shelf.

the disturbance of the biological pump due to the mass extinction will presumably have changed mercury cycling between the surface and deeper ocean reservoirs, though it is unlikely to have affected terrestrial reservoirs significantly.

We therefore used the rate constants and initial reservoir sizes from Amos et al. (2015) and introduced pulses of atmospheric mercury via the model's anthropogenic input parameter. We set the background geogenic (volcanic, hydrothermal, and other natural background sources) mercury input at 90 megagrams per year (Mg/a), consistent with recent estimates of volcanogenic mercury (Amos et al., 2013; Bagnato et al., 2014, 2011). The geogenic background is the primary source of uncertainty in the model, as background mercury flux from volcanism and weathering during this interval is unknown and may include smaller magnitude Deccan eruptions and any persistent non-eruptive volcanic gas release. An increase in the geogenic background would increase the size of all the box model reservoirs; for example, a significantly larger geogenic background of 200 Mg/a leads all reservoirs to increase by a factor of ∼2.2. Consequently, a more massive volcanic pulse is required to enhance the mercury concentrations for geogenic emissions of 200 Mg/a compared to 90 Mg/a. Another critical assumption in the model is the absence of a terrestrial sediment sink. In this study, we assume that the terrestrial sediments sample the concentration of the various terrestrial mercury reservoirs and that the amplitude of any terrestrial sediment sink is small compared to the other fluxes.

For each model run, we calculate an enrichment factor for each of the terrestrial pools and ocean sediment pools. The model enrichment factor is simply the reservoir size at any time-step divided by the initial reservoir size. These terrestrial pools of the mercury model (Smith-Downey et al., 2010) are based on terrestrial carbon cycle pools using the framework of the CASA carbon biogeochemical model (Potter et al., 1993). They are each defined by their residence times: the fast terrestrial carbon pool (primarily organic litter) turns over in about a year, the slow (topsoil) does so in decades, and the armored (deeper soil, sediment) pool in hundreds to thousands of years (Potter et al., 1993). To approximate a fluvial sediment enrichment factor, we calculate a combination of 10% fast, 80% slow, and 10% armored enrichment factors. This combination of fast-slow-armored is because rivers source sediment from topsoil or upper sediment horizons, which generally have appropriate turnover times for the slow pool (Mathieu et al., 2015). Rivers also incorporate organic litter and deeper sediment, so we include 10% fast and armored reservoirs respectively. This choice affects the response rate of the modeled record to the mercury pulse.

Fluid infiltration diffuses mercury concentration over the top few centimeters of riverine wetland sediment at the time of deposition (e.g. Goulet et al., 2007). Iridium Hill Annex and Nirvana have SARs of ∼25 cm/ka and ∼14 cm/ka respectively, and thus with 2 cm of equilibration each sample averages over ∼80–142 yr of mercury deposition. To approximate this diffusion, we apply a moving smoothing window with a width of 125 yr. This also accounts for the size of samples, which are homogenized during preparation. Changing the SAR in the model affects the peak size and duration of mercury enrichment in response to an atmospheric pulse (Fig. 3). This is illustrated by the lower peak enrichment factor for a wider smoothing window (625 yr).

In coastal ocean sediment, bioturbation can lead to mixing on vertical scales of order 5 cm, and potentially much larger. Conservatively, we apply smoothing windows averaging over widths of 2500 yr and 5000 yr to represent SARs of a few cm/ka (Fig. 3). We report the enrichments in terrestrial and marine reservoirs for a variety of pulse sizes, durations, and smoothing window widths in the supplement (Model_tables and Fig. S1).

3.3.2. *Volcanic volatile content estimates*

To estimate the eruptive rate and volume necessary to produce an atmospheric mercury (Hg) pulse, we **(1)** estimate the amount of sulfur dioxide produced concurrently with the mercury, using mean volcanic Hg/SO_2 ratios, then **(2)** use existing Deccan SO_2 per basalt volume estimates from melt inclusions to calculate the corresponding amount of basalt.

Volcanic Hg/SO_2 ratios vary by several orders of magnitude, both between volcanoes and even within the same eruption (e.g. Pyle and Mather, 2003). This is due, at least in part, to differences in partitioning behavior between mercury and sulfur, which may be dependent on temperature or other parameters which vary during the course of an eruption or over the lifetime of a system (Witt et al., 2008). Thus the Hg/SO_2 ratio is a large source of

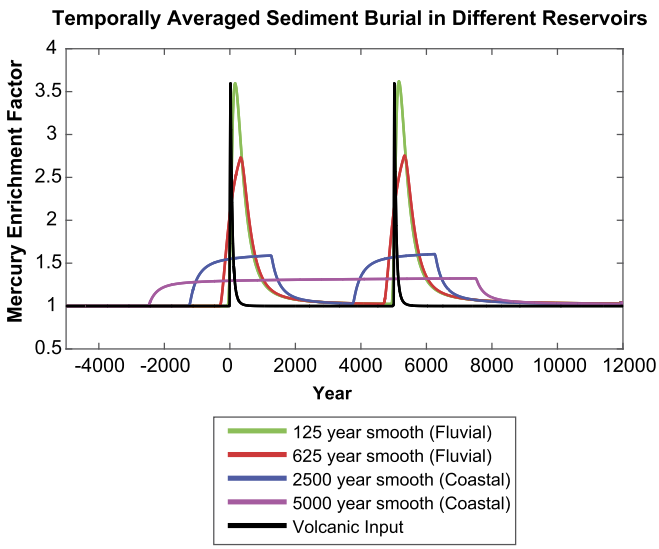

Fig. 3. Modeled mercury enrichment factors for fluvial and coastal marine sediments for typical ranges of sediment accumulation rates, before, during, and after two 2000 Mg/a, 100-year atmospheric Hg pulses. The fluvial sediment is assumed to be dominantly sampling the slow soil reservoir of the box model (Amos et al., 2014). (For interpretation of the colors in the figure(s), the reader is referred to the web version of this article.)

uncertainty for the eruptive volume estimates in comparison to the uncertainties in the box model parameterization. We assume a mean ratio of 5×10^{-6} Hg/S by weight (Fitzgerald and Lamborg, 2014 and references therein), so for example, a pulse of 1000 Mg/a Hg would correspond with the release of 200 Tg S or 400 Tg SO_2 per year. We acknowledge that this estimate may not be correct for Deccan eruptions, either because flood basalts differ from most modern volcanism due to a mantle plume-head source, or because of differences in the composition of the basement rock. The latter is of particular relevance for the Siberian Traps, which was emplaced into volatile-rich sedimentary country rock – potentially releasing non-magmatically sourced mercury (e.g. Saunders, 2016). This is assumed not to be the case for Deccan, which was emplaced dominantly into granitoid rock (e.g. Radhakrishna and Naqvi, 1986).

Each cubic kilometer of basalt is estimated to correspond with the release of several Tg of SO_2. Estimates of the exact amount of SO_2 for Deccan basalt vary, but we use an estimate of 5 Tg SO_2 per km^3 based on the TiO_2-normalized difference in sulfur concentration between Deccan melt inclusions and basalt matrix (Self et al., 2008). A 1000 Mg/a Hg pulse, therefore, corresponds with an eruptive rate of 80 km^3 of basalt per year. For reference, the entire uneroded onshore Deccan basalt volume is estimated to be ~1.3 million km^3 (Jay and Widdowson, 2008).

4. Results

4.1. Mercury concentration chemostratigraphy

Both Iridium Hill Annex (IRA) and Nirvana (NV) have elevated mercury concentration 1000 yr (15 cm) of the Cretaceous-Paleogene boundary (177 ng/g at IRA, 252 ng/g at NV), and there are additional mercury peaks both above and below the boundary (Fig. 4). The background mercury concentration in this interval is approximately 30–50 ng/g at both localities, similar to those predicted by pre-anthropogenic mercury budgets (e.g. Fitzgerald and Lamborg, 2014 and references therein). The peaks correspond to enrichment factors of 3–5 with respect to this background. As the interval analyzed is entirely within the Deccan eruptive period, it is possible that this background is elevated during this entire interval due to smaller ongoing Deccan eruptions or any non-eruptive persistent mercury degassing, including from intrusive magmas via fumaroles (e.g. Witt et al., 2008). If this is the case, larger quantities of mercury are required to cause the observed enrichment factors (Fig. 3).

4.2. Mercury and total organic carbon

There is not generally a strong relationship between mercury and organic carbon in our data (Fig. S2a). Thus the estimated enrichment factors remain ~3–5 when normalized to TOC, with respect to a background of ~15 μg Hg/g OC. While at lower TOC there is a vague relationship between mercury and TOC (Fig. S2b), there is a point at which increasing TOC does not increase mercury deposition, and samples with high TOC (>1%) do not have consistently higher mercury concentrations. The relationship between mercury and TOC, particularly in the geologic record, is known to be complex (e.g. Grasby et al., 2013; Percival et al., 2018; Sanei et al., 2012) and presumably a function of the type of organic material in addition to the availability of sulfides, clays, or other materials with which mercury can be deposited. These factors lead to some unquantifiable uncertainty in our enrichment factors.

4.3. Box model eruption size estimates

Eruptions are modeled as mercury pulses using a modern mercury cycle box model (Amos et al., 2013). These pulses cause inflation of the modeled global mercury budget and an increase in each of the modeled reservoirs. We also apply a smoothing window to the modeled terrestrial record, based on SAR (see section 3.3). High enrichment factors are caused by a high rate of mercury emission, long duration of a pulse, or both. A range of mercury pulse sizes could cause terrestrial enrichment factors of 3–5: ~2000–3000 Mg/a for ~100-year eruptions, or longer events of smaller magnitude, e.g. a 500 Mg/a pulse for ~1000 yr.

To further constrain the eruptive duration, we consider how much time is needed for an individual pulse of atmospheric mercury to be completely deposited into sediment. Using the same box model, we plot the total environmental enrichment for 1500 yr, during and after a century-long 2000 Mg Hg/a eruption, along with the proportion of the enrichment in each reservoir (Fig. 5a, b, c). It can be seen that increased mercury deposition in terrestrial systems lasts a maximum of a thousand years post eruption (Fig. 5c). As consecutive samples with elevated mercury are rare within the 1–2 ka resolution record, we infer that these individual eruptions lasted a few centuries, and no longer than ~500 yr. At a 500 yr duration or longer, one would expect the eruption to cause elevated mercury concentrations in multiple consecutive samples. This additional constraint now limits the range to 100-year events emitting pulses of 2000–3000 Mg/a to 500-year events emitting 500–1000 Mg/a.

Approximately 12.5 Mg mercury is released per cubic kilometer of basalt erupted, using an average volcanic mercury to sulfur ratio (Bagnato et al., 2014; Fitzgerald and Lamborg, 2014) along with estimates of Deccan sulfur content from melt inclusions (Schmidt et al., 2016; Self et al., 2008) (see section 3.3). Peak terrestrial enrichment factors of 3–5 then suggest eruptive rates of ~40–80 km^3/a for 500-year events and ~160–240 km^3/a for 100-year events (Fig. 6), resulting in maximum eruptive volumes of 16,000–40,000 km^3. There are ~10 peaks in our record, resulting in a cumulative 160,000–400,000 km^3 of basalt, which is within an order of magnitude of the independent estimate of ~150,000–200,000 km^3 of basalt emplaced in the first ~100 ka of the Paleocene (Jay and Widdowson, 2008; Schoene et al., 2019; Sprain et al., 2019). These field-based volume estimates are likely

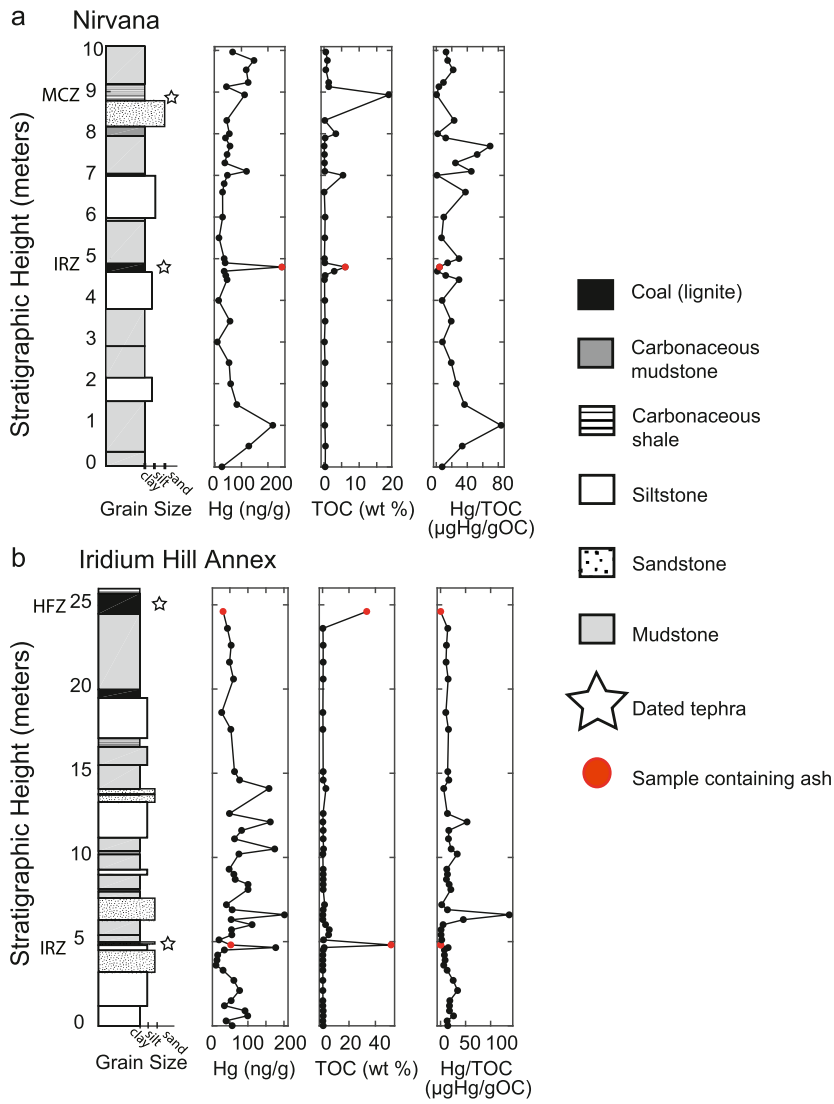

Fig. 4. Stratigraphic sections, mercury (Hg), total organic carbon (TOC), and Hg/TOC data for both localities analyzed in this study.

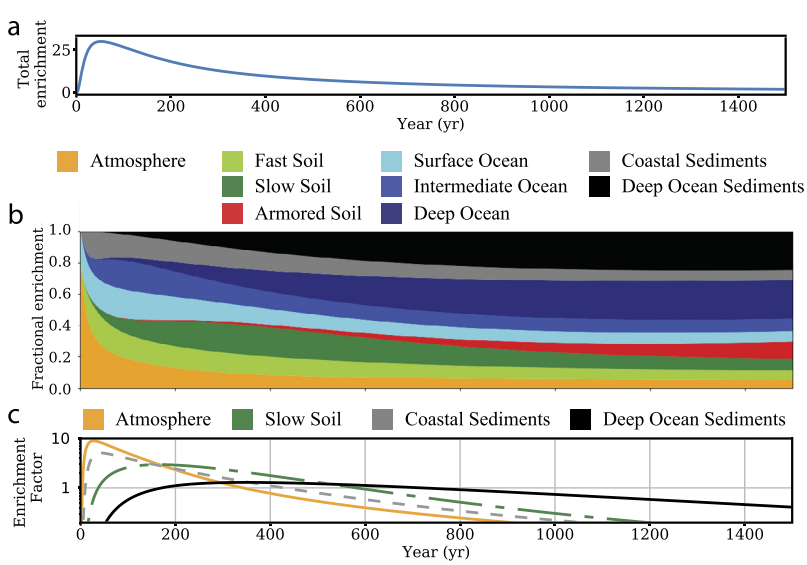

Fig. 5. a) Total environmental mercury enrichment (above background) summed over all reservoirs through time following a Deccan-scale 2000 Mg/a, 100-year atmospheric mercury pulse input into a modern mercury box model (Amos et al., 2014). **b)** The proportion of the total enrichment within each reservoir following the same atmospheric mercury pulse. **c)** The enrichment factors (above background) in the atmospheric reservoir, terrestrial fast and slow soil reservoirs, and marine coastal and deep ocean sediment reservoirs following the same atmospheric mercury pulse.

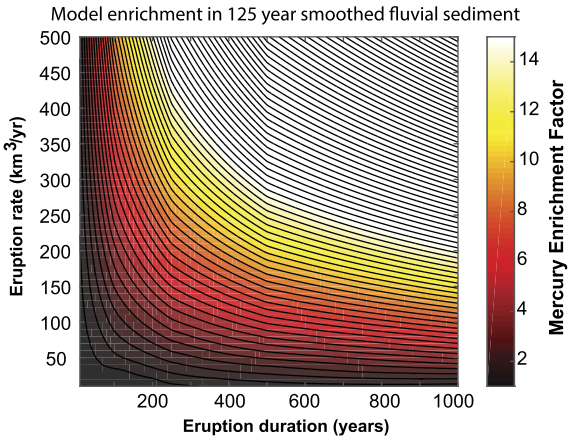

Fig. 6. Mercury enrichment factors in the terrestrial reservoir, with 125 yr sediment averaging, for a range of eruptive volumes and durations.

lower bounds since an uncertain, but presumably large, amount of Deccan Traps basalt has been eroded in India's tropical environment over the last 66 Ma.

5. Discussion

5.1. Potential Hg sources

There are a few non-Deccan potential mercury sources: a) sedimentary (fluid remobilization) effects, b) local volcanism, or remobilization of sedimentary/biomass mercury due to c) wildfires, or d) via changes in weathering. We do not believe these are the dominant mercury sources for the following reasons:

5.1.1. Sedimentary effects

The presence of similar size mercury concentration peaks at both localities demonstrates that these are at least regional signals, rather than due to any local sedimentary/fluid remobilization effect. Additionally, we have ruled out variation due to changes in organic carbon concentration, and there is no visible pyrite, including within lignites, suggesting that sulfides are not the primary control on mercury concentrations.

5.1.2. Local volcanic eruptions

Local volcanic eruptions, from the Bitterroot Lobe of the Idaho Batholith (Ickert et al., 2015), frequently occur during the Cretaceous and Paleocene. Several samples contain tephra from these eruptions, as well as immediately surrounding sediment. However, these samples do not record elevated mercury concentrations (Fig. S1). The only exception is the Nirvana sample, which contains the IrZ tephra layer as well as the Cretaceous-Paleogene boundary clay.

We believe this lack of signal to be due to the short duration of the local eruptions. As mercury equilibrates over a few centimeters of sediment post-deposition (e.g. Goulet et al., 2007), short duration pulses in atmospheric mercury are only likely to be preserved if they are very large, the SAR is very high, and/or the record is sampled at a resolution within about an order of magnitude of the duration of the pulse. This is apparent when examining Quaternary records. Mercury peaks caused by arc volcanism and local wildfires (presumably all <1-year duration events) have been found in recent lake sediments with an average SAR of 37.5 cm/ka, sampled at a resolution of every ~20 yr (Daga et al., 2016). Conversely, a Quaternary marine sedimentary mercury record with an average SAR of 7 cm/ka, sampled at a 1000–2000 yr resolution (Kita et al., 2016), does not record the large volume, but short duration, Toba (5300 km^3, ~74 ka; (Costa et al., 2014)) and Bishop Tuff (~600 km^3, ~760 ka; (Hildreth and Wilson, 2007)) eruptions.

While the terrestrial sediment records compiled in this study have high average SARs (14, 25 cm/ka), we are sampling them at a resolution of every 1000–2000 yr. The local arc volcanic eruptions did not last longer than a few days to months, and the frequency of very large (>100 km^3) eruptions likely did not exceed once every several thousand years (e.g. Papale, 2018). In order to be preserved as significant anomalies at this resolution, eruptions need to be at least ~100 yr in duration, longer than the <1 yr local eruptions.

5.1.3. Wildfires

Fires remobilize mercury taken up by biomass from the atmosphere and redistribute it (Friedli et al., 2009). Similar to the local volcanic eruptions, wildfires are likely to be short duration events (<1 yr) and as such are smoothed out over centuries once deposited in the sedimentary record. These small local events are not likely to cause significant perturbations in a 1000–2000 yr resolution record. It is possible that peaks correspond with much larger fire events. However, western North America does not record a strong/visible presence of charcoal in this time interval (Belcher et al., 2003), and the Cretaceous-Paleogene boundary does not record polycyclic aromatic hydrocarbons (PAH) indicative of massive wildfires (Belcher et al., 2009). Additionally, there is no indication of globally significant wildfires in the earliest Paleocene in PAH records from Europe (Arinobu et al., 1999).

5.1.4. Weathering

Changes in weathering can also redistribute sedimentary mercury (e.g. Them et al., 2019). While changes in weathering may contribute to aggregate effects, particularly in oceans where the sediment and mercury are tied to continent-scale sources, our sediment catchment is comparatively small. In order to increase the concentration of mercury via increased weathering, a substantial amount of the mercury in weathered rock would need to be rapidly dissolved, and re-deposited locally. This process is most efficient when the rock fragments are entirely in suspension and even then only a fraction (generally <20% in 24 h) of the mercury is re-dissolved (Gibson et al., 2015). Therefore in order to cause a factor of 3–5 increase in mercury for 100 yr, the amount of material weathered is required to at least triple, and more likely increase by 15 times or more. While that may be the case right at the boundary, coincident with destabilization of floral ecosystems (Vajda and McLoughlin, 2004), there is no evidence of strongly enhanced weathering occurring thousands of years into the Paleogene.

5.2. Box model assumptions

The modeling framework we have utilized has a combination of strengths and drawbacks. One major strength is that the box model incorporates biogeochemical recycling instead of assuming that sediments are passively collecting mercury from the atmosphere and retaining all of it. The model results demonstrate that even though volcanogenic mercury may not be immediately deposited in the sediment, large pulses do cause increases in mercury concentration in all reservoirs on a timescale that should be capable of preservation in the geologic record.

A significant assumption in the model framework is the use of a constant SAR, which may not be the case in a terrestrial floodplain environment. The dependency on this assumption is due to using a moving average to approximate equilibration of mercury over 2 cm of sediment, to simulate both in-lab sample homogenization and fluid infiltration at the time of deposition. This results in the same mercury pulse causing a smaller enrichment in environments with lower SARs, and vice versa (Fig. 3). This effect is also crucial for

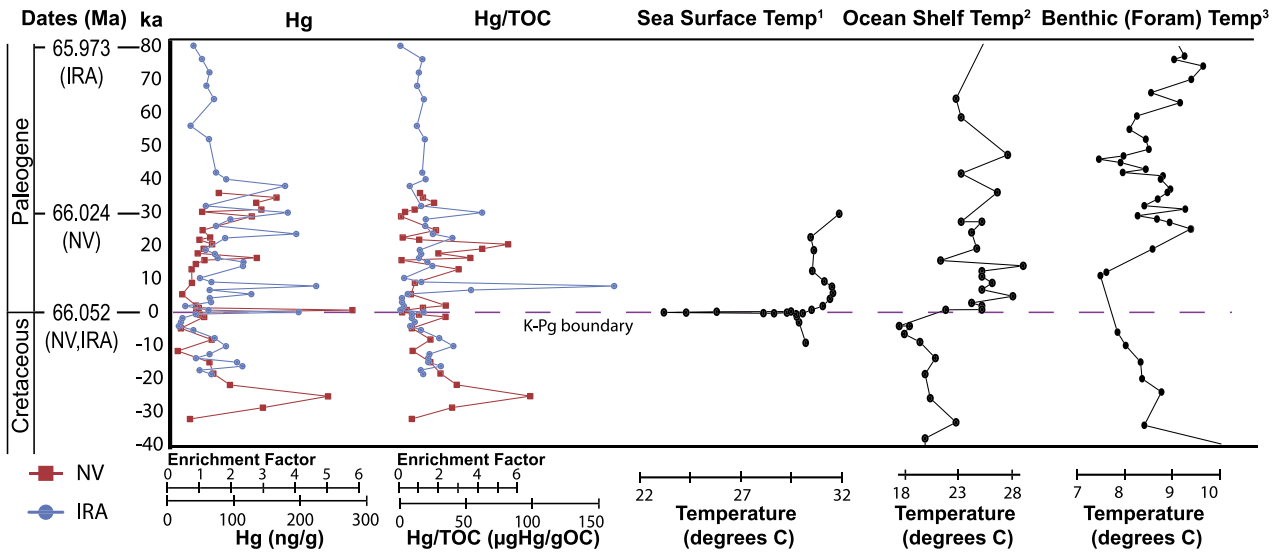

Fig. 7. Mercury (Hg) and mercury/total organic carbon (Hg/TOC) for Iridium Hill Annex (IRA) and Nirvana (NV) Cretaceous-Paleogene boundary localities compared to several high-resolution temperature records. Dates for IRA and NV from Sprain et al. (2015, 2018). 1: Tex86 derived sea surface temperature from Brazos River, USA (Vellekoop et al., 2014). 2: Temperature derived from oxygen isotope composition of fish debris from El Kef, Tunisia (MacLeod et al., 2018). 3: Temperature derived from oxygen isotope composition of benthic foraminifers (*Nuttallides*) from IODP 1262 (Barnet et al., 2017).

marine records, where the deposition process of mercury can be complicated due to ocean currents, water depth, and ocean mixing time (e.g. Lamborg et al., 2014).

Another complicating factor is that although large emissions of gaseous mercury are distributed globally, they are distributed unevenly (e.g. Chen et al., 2018). This contributes to differences between mercury records from different locations, and uncertainty in eruption size estimates. Therefore perhaps less Deccan mercury was deposited in Montana than predicted by the box model, as Montana and India are on opposite sides of the globe and were in opposite hemispheres during the Cretaceous.

5.3. Comparison of Cretaceous-Paleogene mercury records

The mercury enrichment factors (multiple of locality-specific background Hg/TOC) calculated for each record are used to test consistency between different mercury records as well as with the estimated eruption sizes. Our modeling framework illustrates that the SAR and sampling resolution must be explicitly considered when comparing mercury records. The response time to a mercury pulse is similar for both coastal marine sediments and terrestrial sediments (Fig. 5c). However, SARs are frequently lower in marine environments, leading to a lower expected enrichment factor for a given eruption size. Sampling resolution is equally important, as mercury tends to be deposited rapidly into sediments – within about an order of magnitude of the pulse duration (Fig. 5a). Therefore records sampled at millennial scale resolution have the highest likelihood of capturing eruptions which each lasted several hundred to a thousand years. Eruptive events of the proposed scale may be captured in records with lower sampling resolution, but they are likely to have smaller enrichment factors and fewer peaks, as the odds of sampling the moment of peak enrichment decrease. Most mercury records show higher enrichment factors when the sampling resolution is higher (Font et al., 2016; Keller et al., 2018; Percival et al., 2018; Sial et al., 2016).

The peak enrichment factors are similar between the Nirvana and Iridium Hill Annex localities, which supports the interpretation that they are caused by eruptive events of similar magnitude (Fig. 7). These estimates of eruption size are also generally consistent with the mercury enrichment factors of other Cretaceous-Paleogene mercury chemostratigraphies. The Seymour Island record, which has a comparable SAR of 20 cm/ka and sampling resolution of ∼2500 yr, has Hg/TOC enrichment factors of ∼3 in peaks close to the boundary (Percival et al., 2018). The Gilbert Creek locality within the Hell Creek Formation presumably has a similar SAR, although the exact chronology is uncertain (Percival et al., 2018). Peak Hg/TOC enrichment factors at Gilbert Creek are 5–6 in the late Cretaceous, with smaller peaks closer to the boundary, although the lack of a definitive IrZ tephra layer makes correlation with our records uncertain (Percival et al., 2018).

Coastal marine sediments with SARs of a few cm/ka, utilizing a smoothing window of 2500 yr, are expected to have enrichment factors of 2–3 for the estimated eruption volumes (Supplementary Fig. 1b). This is consistent with observed Hg/TOC enrichments in marine localities. Bass River (ODP Leg 174AX) has SAR of ∼1 cm/ka, a sampling interval of ∼7500 years, and correspondingly low enrichment factors of 1.5 to 2 (Percival et al., 2018). Elles, El Kef, and Bidart have enrichment factors of 2–4, SARs of approximately 1–4 cm/ka, and sampling resolutions of ∼2000–5000 yr (Font et al., 2016; Keller et al., 2018; Vonhof and Smit, 1997). Bottaccione and Stevns Klint have SARs of approximately 1 and 4 cm/kyr respectively, and enrichment factors of perhaps 3, however the limited datasets make determining the background Hg/TOC difficult (Gilleaudeau et al., 2018; Sial et al., 2016; Sinnesael et al., 2016). Bottaccione has frequently low (<1 ng/g) mercury concentrations, which suggests availability in the water column may not control preservation. These comparisons exclude peaks at the boundary, and enrichment factors are calculated with respect to Deccan interval background for each locality. We have excluded records lacking TOC measurements or without robust age models, as well as Zumaia, where mercury deposition is strongly linked with sediment fluxes (Percival et al., 2018).

These records differ with respect to the timing of mercury peaks because it is unlikely that every record is capturing the same specific eruptions. This is true even for the Nirvana and Iridium Hill Annex records, despite their close proximity, comparable SARs, and sampling resolutions. The average time between the emission of a gaseous mercury pulse and ultimate burial in sediment is approximately 1000 yr, and the peak enrichment factor in the modeled slow soil and coastal marine reservoirs is only reached for less than 500 yr (Fig. 5). Thus, unless the time interval captured in each sample is synchronous between localities to

within 500 yr, the records will not be identical. Additionally, due to the inherently discontinuous nature of the sedimentary record at the century scale, even continuously sampled records from different localities would be unlikely to record the same eruptions. The stochasticity of sedimentation and the aliasing effects of sampling ensure that no two records would correlate perfectly.

5.4. Implications for Deccan volcanism and climate

We have estimated, based on our mercury analyses, that these Deccan eruptions consisted of basalt fluxes between ∼40–80 km^3/a for 500-year events and ∼160–240 km^3/a for 100-year events (Fig. 6). Flood basalt eruptions have been independently hypothesized to be of the order of 10^3–10^4 km^3 in volume (Self et al., 2006) therefore we believe our mercury-based estimates of 16,000-40,000 km^3 per eruption (or series of closely spaced individual eruptions) to be reasonable. Additionally, there likely were more eruptions within this time interval than peaks in the records. Although biogeochemical recycling of mercury does extend the deposition time of pulses, shorter duration (≤100 yr) events of smaller magnitude may not be captured at our 1000–2000 yr sampling resolution or will correspond to low enrichment factors. While it is thus difficult to estimate the minimum hiatus duration, these records indicate a maximum of 10,000 yr between each eruption for the interval spanning 30 ka prior to and post-Cretaceous-Paleogene boundary.

Although we attribute the majority of our peaks to Deccan volcanism, we suggest that the mercury peak very close to the Cretaceous-Paleogene boundary, which is the largest in nearly every mercury record for this time interval (e.g. Sial et al., 2016; Keller et al., 2018; Percival et al., 2018), is at least partly due to the Chicxulub impact. The Chicxulub impact released ∼94,000–480,000 Mg mercury instantaneously, based on the mass of evaporites vaporized and an assumed concentration of 40 ng/g mercury (Artemieva and Morgan, 2017; Fitzgerald and Lamborg, 2014). This corresponds with enrichment factors of at least 20 in coastal marine sediments and 4–15 in terrestrial sediments (see supplement for details). At both localities in this study, this peak (4–6 × background) falls within a coal seam, so it is not visible when normalized to TOC. However, we do not see similarly high values in either of two other coal seams within our sections, and as other mercury records also have high values coincident with the boundary, this peak is most likely due to atmospheric mercury increase. An increase in weathering at the boundary may also contribute to this peak, or local sedimentary effects in sections where the boundary is coincident with a significant lithology change (Percival et al., 2018).

The Deccan eruptions of the size indicated by the other mercury peaks have the potential to cause sulfate aerosol driven climate cooling. A mercury pulse of 500–3000 Mg/a (240 km^3/a basalt) corresponds to a release of 200–1200 Tg/a SO_2, using, as before, an average volcanic Hg/S ratio of 5×10^{-6} by weight (Fitzgerald and Lamborg, 2014 and references therein). Climate models indicate that similar rates of sulfur release would cause cooling of ∼1–6 °C for the duration of the eruption (Schmidt et al., 2016). This model estimate assumes all SO_2 emitted enters the stratosphere, although this may be an overestimate (Glaze et al., 2017). This cooling may contribute to variability in climate records and to the immediate post boundary cool period. However, it is not clearly seen (Fig. 7), consistent with the eruptions being less than 500 yr in duration. Despite the lack of geologic preservation, several centuries of cooling at least every 10,000 yr may be sufficient to perturb ecological and climatological systems significantly.

Other studies demonstrate that eruptions of approximately this size are not likely to have caused CO_2 driven warming individually, but with less than 10,000-year hiatuses between them could have cumulatively contributed to warming (e.g. Tobin et al., 2016). The timing of these eruptions indicates that eruptive CO_2 likely contributed to the immediate post-boundary warming seen in several records (Fig. 7) (MacLeod et al., 2018; Vellekoop et al., 2014) however it is unlikely that the eruptions are large enough to be the primary cause. There is, therefore, no clear correlation between Deccan Traps eruptions and climate records on a sub-100 ka scale, even during the interval hypothesized to contain the largest volume Deccan eruptions (Schoene et al., 2019; Sprain et al., 2019). Sub-1000 year resolution climate records have the potential to record these brief colder periods and address this inconsistency.

6. Conclusions

Periods of higher mercury concentration indicative of Deccan eruptions occur within 30 ka both prior to and post the Cretaceous-Paleogene boundary. Utilizing a global mercury box model, we estimate that the mercury peaks correspond to eruptions with magma output fluxes of 40–240 km^3/a, which lasted 100–500 years, and occurred at least every 10,000 yr. This demonstrates that mercury chemostratigraphy can be used as a tool to quantitatively assess flood basalt eruptive dynamics. Deccan eruptions of the estimated size are hypothesized to have released enough SO_2 to cause significant (∼1–6 °C) cooling for their duration. However, with a duration of less than 1000 yr, these cooler periods are not long enough to be unambiguously preserved in most available climate records. Higher resolution climate records, or statistical analyses of existing records, are needed in order to evaluate whether these cool periods occurred. Nevertheless, if the cooler periods occurred as hypothesized, the repeated significant climatic perturbations within 50 ka of the Cretaceous-Paleogene boundary may have contributed to ecological changes.

Author contributions

I.F. collected and analyzed samples and data, and generated and interpreted box model results. T.M. participated in data interpretation and generated and interpreted box model results. C.S. and T.T. collected samples and participated in the interpretation of results. M.M.-D. analyzed samples and participated in the interpretation of results. P.R. participated in interpretation of results. All authors participated in writing and editing the manuscript.

Acknowledgements

We would like to thank three anonymous reviewers, as well as Steve Self, for valuable comments on the manuscript. Thanks to L.N. Weaver, C.B. Keller, G. Quaresma, J. Anderson, and the Hell Creek Project for fieldwork assistance. This work was funded by NSF EAR-1615021 and the Esper S. Larsen Fund of the University of California Berkeley. Field work was supported by Paleontological Society Kenneth E & Annie Caster and Stephen Jay Gould Awards, a Geological Society of America Graduate Student Research Grant, and a Sigma Xi Grant in Aid of Research. I.F. is supported by an NSF Graduate Research Fellowship.

Appendix A. Supplementary material

Supplementary material related to this article can be found online at https://doi.org/10.1016/j.epsl.2019.115721.

References

Alvarez, L.W., 1983. Experimental evidence that an asteroid impact led to the extinction of many species 65 million years ago. Proc. Natl. Acad. Sci. 80, 627–642. https://doi.org/10.1073/pnas.80.2.627.

Amos, H.M., Jacob, D.J., Kocman, D., Horowitz, H.M., Zhang, Y., Dutkiewicz, S., Horvat, M., Corbitt, E.S., Krabbenhoft, D.P., Sunderland, E.M., 2014. Global biogeochemical implications of Mercury discharges from rivers and sediment burial. Environ. Sci. Technol. 48, 9514–9522. https://doi.org/10.1021/es502134t.

Amos, H.M., Jacob, D.J., Streets, D.G., Sunderland, E.M., 2013. Legacy impacts of all-time anthropogenic emissions on the global mercury cycle. Glob. Biogeochem. Cycles 27, 410–421. https://doi.org/10.1002/gbc.20040.

Amos, H.M., Sonke, J.E., Obrist, D., Robins, N., Hagan, N., Horowitz, H.M., Mason, R.P., Witt, M., Hedgecock, I.M., Corbitt, E.S., Sunderland, E.M., 2015. Observational and modeling constraints on global anthropogenic enrichment of mercury. Environ. Sci. Technol. 49, 4036–4047. https://doi.org/10.1021/es5058665.

Archer, D., Eby, M., Brovkin, V., Ridgwell, A., Cao, L., Mikolajewicz, U., Caldeira, K., Matsumoto, K., Munhoven, G., Montenegro, A., Tokos, K., 2009. Atmospheric lifetime of fossil fuel carbon dioxide. Annu. Rev. Earth Planet. Sci. 37, 117–134. https://doi.org/10.1146/annurev.earth.031208.100206.

Arens, N.C., Thompson, A., Jahren, A.H., 2014. A preliminary test of the press-pulse extinction hypothesis: palynological indicators of vegetation change preceding the Cretaceous-Paleogene boundary, McCone County, Montana, USA. Spec. Pap., Geol. Soc. Am. 503, 209–227. https://doi.org/10.1130/2014.2503(07).

Arinobu, T., Ishiwatari, R., Kaiho, K., Lamolda, M.A., 1999. Spike of pyrosynthetic polycyclic aromatic hydrocarbons associated with an abrupt decrease in δ^{13}C of a terrestrial biomarker at the Cretaceous-Tertiary boundary at Caravaca, Spain. Geology 27, 723–726. https://doi.org/10.1130/0091-7613(1999)027<0723:SOPPAH>2.3.CO;2.

Artemieva, N., Morgan, J., 2017. Quantifying the release of climate-active gases by large meteorite impacts with a case study of Chicxulub. Geophys. Res. Lett. 44, 10,180–10,188. https://doi.org/10.1002/2017GL074879.

Bagnato, E., Aiuppa, A., Parello, F., Allard, P., Shinohara, H., Liuzzo, M., Giudice, G., 2011. New clues on the contribution of Earth's volcanism to the global mercury cycle. Bull. Volcanol. 73, 497–510. https://doi.org/10.1007/s00445-010-0419-y.

Bagnato, E., Tamburello, G., Avard, G., Martinez-Cruz, M., Enrico, M., Fu, X., Sprovieri, M., Sonke, J.E., 2014. Mercury fluxes from volcanic and geothermal sources: an update. Geol. Soc. (Lond.) Spec. Publ. 410. https://doi.org/10.1144/SP410.2.

Barnet, J.S.K., Littler, K., Kroon, D., Leng, M.J., Westerhold, T., Röhl, U., Zachos, J.C., 2017. A new high-resolution chronology for the late Maastrichtian warming event: establishing robust temporal links with the onset of Deccan volcanism. Geology 46, 147–150. https://doi.org/10.1130/G39771.1.

Belcher, C.M., Collinson, M.E., Sweet, A.R., Hildebrand, A.R., Scott, A.C., 2003. Fireball passes and nothing burns—the role of thermal radiation in the Cretaceous-Tertiary event: evidence from the charcoal record of North America. Geology 31, 1061–1064. https://doi.org/10.1130/G19989.1.

Belcher, C.M., Finch, P., Collinson, M.E., Scott, A.C., Grassineau, N.V., 2009. Geochemical evidence for combustion of hydrocarbons during the K-T impact event. Proc. Natl. Acad. Sci. 106, 4112–4117. https://doi.org/10.1073/pnas.0813117106.

Black, B.A., Neely, R.R., Lamarque, J.F., Elkins-Tanton, L.T., Kiehl, J.T., Shields, C.A., Mills, M.J., Bardeen, C., 2018. Systemic swings in end-Permian climate from Siberian Traps carbon and sulfur outgassing. Nat. Geosci. https://doi.org/10.1038/s41561-018-0261-y.

Chen, L., Zhang, W., Zhang, Y., Tong, Y., Liu, M., Wang, H., Xie, H., Wang, X., 2018. Historical and future trends in global source-receptor relationships of mercury. Sci. Total Environ. 610–611, 24–31. https://doi.org/10.1016/j.scitotenv.2017.07.182.

Cossa, D., Coquery, M., Gobeil, C., Martin, J.-M., 1996. Mercury fluxes at the Ocean Margins BT. In: Baeyens, W., Ebinghaus, R., Vasiliev, O. (Eds.), Global and Regional Mercury Cycles: Sources, Fluxes and Mass Balances. Springer Netherlands, Dordrecht, pp. 229–247.

Costa, A., Smith, V.C., Macedonio, G., Matthews, N.E., 2014. The magnitude and impact of the Youngest Toba Tuff super-eruption. Front. Earth Sci. 2, 16. https://doi.org/10.3389/feart.2014.00016.

Daga, R., Ribeiro Guevara, S., Pavlin, M., Rizzo, A., Lojen, S., Vreča, P., Horvat, M., Arribére, M., 2016. Historical records of mercury in southern latitudes over 1600 years: lake Futalaufquen, Northern Patagonia. Sci. Total Environ. 553, 541–550. https://doi.org/10.1016/j.scitotenv.2016.02.114.

Driscoll, C.T., Han, Y.-J., Chen, C.Y., Evers, D.C., Lambert, K.F., Holsen, T.M., Kamman, N.C., Munson, R.K., 2007. Mercury contamination in forest and freshwater ecosystems in the Northeastern United States. Bioscience 57, 17–28. https://doi.org/10.1641/B570106.

Fastovsky, D.E., Bercovici, A., 2016. The Hell Creek Formation and its contribution to the Cretaceous–Paleogene extinction: a short primer. Cretac. Res. 57, 368–390. https://doi.org/10.1016/j.cretres.2015.07.007.

Fitzgerald, W.F., Lamborg, C.H., 2014. 11.4. Geochemistry of Mercury in the environment. In: Holland, H., Turekian, K. (Eds.), Treatise on Geochemistry, second edition. Elsevier, Oxford, pp. 91–129.

Font, E., Adatte, T., Sial, A.N., de Lacerda, L.D., Keller, G., Punekar, J., 2016. Mercury anomaly, Deccan volcanism, and the end-Cretaceous mass extinction. Geology 44, 171–174. https://doi.org/10.1130/G37451.1.

Friedli, H.R., Arellano, A.F., Cinnirella, S., Pirrone, N., 2009. Initial estimates of mercury emissions to the atmosphere from global biomass burning. Environ. Sci. Technol. 43, 3507–3513. https://doi.org/10.1021/es802703g.

Gibson, B.D., Ptacek, C.J., Blowes, D.W., Daugherty, S.D., 2015. Sediment resuspension under variable geochemical conditions and implications for contaminant release. J. Soils Sediments 15, 1644–1656. https://doi.org/10.1007/s11368-015-1106-6.

Gilleaudeau, G.J., Voegelin, A.R., Thibault, N., Moreau, J., Ullmann, C.V., Klaebe, R.M., Korte, C., Frei, R., 2018. Stable isotope records across the Cretaceous-Paleogene transition, Stevns Klint, Denmark: new insights from the chromium isotope system. Geochim. Cosmochim. Acta 235, 305–332. https://doi.org/10.1016/j.gca.2018.04.028.

Glaze, L.S., Self, S., Schmidt, A., Hunter, S.J., 2017. Assessing eruption column height in ancient flood basalt eruptions. Earth Planet. Sci. Lett. 457, 263–270. https://doi.org/10.1016/j.epsl.2014.07.043.

Goulet, R.R., Holmes, J., Page, B., Poissant, L., Siciliano, S.D., Lean, D.R.S., Wang, F., Amyot, M., Tessier, A., 2007. Mercury transformations and fluxes in sediments of a riverine wetland. Geochim. Cosmochim. Acta 71, 3393–3406. https://doi.org/10.1016/j.gca.2007.04.032.

Grasby, S.E., Sanei, H., Beauchamp, B., Chen, Z., 2013. Mercury deposition through the Permo–Triassic Biotic Crisis. Chem. Geol. 351, 209–216. https://doi.org/10.1016/j.chemgeo.2013.05.022.

Hildreth, W., Wilson, C.J.N., 2007. Compositional zoning of the Bishop Tuff. J. Petrol. 48, 951–999. https://doi.org/10.1093/petrology/egm007.

Ickert, R.B., Mulcahy, S.R., Sprain, C.J., Banaszak, J.F., Renne, P.R., 2015. Chemical and Pb isotope composition of phenocrysts from bentonites constrains the chronostratigraphy around the Cretaceous-Paleogene boundary in the Hell Creek region. Montana. Geochem. Geophys. Geosyst. 16, 2743–2761. https://doi.org/10.1002/2015GC005898.

Jay, A.E., Widdowson, M., 2008. Stratigraphy, structure and volcanology of the SE Deccan continental flood basalt province: implications for eruptive extent and volumes. J. Geol. Soc. Lond. 165, 177–188. https://doi.org/10.1144/0016-76492006-062.

Keller, G., Mateo, P., Punekar, J., Khozyem, H., Gertsch, B., Spangenberg, J., Bitchong, A.M., Adatte, T., 2018. Environmental changes during the Cretaceous-Paleogene mass extinction and Paleocene-Eocene Thermal Maximum: implications for the Anthropocene. Gondwana Res. 56, 69–89. https://doi.org/10.1016/j.gr.2017.12.002.

Kita, I., Yamashita, T., Chiyonobu, S., Hasegawa, H., Sato, T., Kuwahara, Y., 2016. Mercury content in Atlantic sediments as a new indicator of the enlargement and reduction of Northern Hemisphere ice sheets. J. Quat. Sci. 31, 167–177. https://doi.org/10.1002/jqs.2854.

Lamborg, C.H., Hammerschmidt, C.R., Bowman, K.L., Swarr, G.J., Munson, K.M., Ohnemus, D.C., Lam, P.J., Heimbürger, L.-E., Rijkenberg, M.J.A., Saito, M.A., 2014. A global ocean inventory of anthropogenic mercury based on water column measurements. Nature 512, 65. https://doi.org/10.1038/nature13563.

Lugato, E., Smith, P., Borrelli, P., Panagos, P., Ballabio, C., Orgiazzi, A., Fernandez-Ugalde, O., Montanarella, L., Jones, A., 2018. Soil erosion is unlikely to drive a future carbon sink in Europe. Sci. Adv. 4, eaau3523. https://doi.org/10.1126/sciadv.aau3523.

MacLeod, K.G., Quinton, P.C., Sepúlveda, J., Negra, M.H., 2018. Postimpact earliest Paleogene warming shown by fish debris oxygen isotopes (El Kef, Tunisia). Science 360 (6396). https://doi.org/10.1126/science.aap8525.

Mathieu, J.A., Hatté, C., Balesdent, J., Parent, É., 2015. Deep soil carbon dynamics are driven more by soil type than by climate: a worldwide meta-analysis of radiocarbon profiles. Glob. Change Biol. 21, 4278–4292. https://doi.org/10.1111/gcb.13012.

Olund, S.D., DeWild, J.F., Olson, M.L., Tate, M.T., 2004. Methods for the Preparation and Analysis of Solids and Suspended Solids for Total Mercury. Techniques and Methods.

Papale, P., 2018. Global time-size distribution of volcanic eruptions on Earth. Sci. Rep. 8, 6838. https://doi.org/10.1038/s41598-018-25286-y.

Percival, L.M.E., Jenkyns, H.C., Mather, T.A., Dickson, A.J., Batenburg, S.J., Ruhl, M., Hesselbo, S.P., Barclay, R., Jarvis, I., Robinson, S.A., Woelders, L., 2018. Does large igneous province volcanism always perturb the mercury cycle? Comparing the records of Oceanic Anoxic Event 2 and the end-Cretaceous to other Mesozoic events. Am. J. Sci. 318, 799–860. https://doi.org/10.2475/08.2018.01.

Percival, L.M.E., Witt, M.L.I., Mather, T.A., Hermoso, M., Jenkyns, H.C., Hesselbo, S.P., Al-Suwaidi, A.H., Storm, M.S., Xu, W., Ruhl, M., 2015. Globally enhanced mercury deposition during the end-Pliensbachian extinction and Toarcian OAE: a link to the Karoo–Ferrar Large Igneous Province. Earth Planet. Sci. Lett. 428, 267–280. https://doi.org/10.1016/j.epsl.2015.06.064.

Potter, C.S., Randerson, J.T., Field, C.B., Matson, P.A., Vitousek, P.M., Mooney, H.A., Klooster, S.A., 1993. Terrestrial ecosystem production: a process model based on global satellite and surface data. Glob. Biogeochem. Cycles 7, 811–841. https://doi.org/10.1029/93GB02725.

Pyle, D.M., Mather, T.A., 2003. The importance of volcanic emissions for the global atmospheric mercury cycle. Atmos. Environ. 37, 5115–5124. https://doi.org/10.1016/j.atmosenv.2003.07.011.

Radhakrishna, B.P., Naqvi, S.M., 1986. Precambrian continental crust of India and its evolution. J. Geol. 94, 145–166. https://doi.org/10.1086/629020.

Renne, P.R., Deino, A.L., Hilgen, F.J., Kuiper, K.F., Mark, D.F., Mitchell, W.S., Morgan, L.E., Mundil, R., Smit, J., 2013. Time scales of critical events around the Cretaceous-Paleogene boundary. Science 339, 684–687. https://doi.org/10.1126/science.1230492.

Sanei, H., Grasby, S.E., Beauchamp, B., 2012. Latest Permian mercury anomalies. Geology 40, 63–66. https://doi.org/10.1130/G32596.1.

Saunders, A.D., 2016. Two LIPs and two Earth-system crises: the impact of the North Atlantic Igneous Province and the Siberian Traps on the Earth-surface carbon cycle. Geol. Mag. 153, 201–222. https://doi.org/10.1017/S0016756815000175.

Schmidt, A., Skeffington, R.A., Thordarson, T., Self, S., Forster, P.M., Rap, A., Ridgwell, A., Fowler, D., Wilson, M., Mann, G.W., Wignall, P.B., Carslaw, K.S., 2016. Selective environmental stress from sulphur emitted by continental flood basalt eruptions. Nat. Geosci. 9, 77–82. https://doi.org/10.1038/ngeo2588.

Schoene, B., Eddy, M.P., Samperton, K.M., Keller, C.B., Keller, G., Adatte, T., Khadri, S.F.R., 2019. U–Pb constraints on pulsed eruption of the Deccan Traps across the end-Cretaceous mass extinction. Science 363 (6429), 862–866. https://doi.org/10.1126/science.aau2422.

Schulte, P., Alegret, L., Arenillas, I., Arz, J.A., Barton, P.J., Bown, P.R., Bralower, T.J., Christeson, G.L., Claeys, P., Cockell, C.S., Collins, G.S., Deutsch, A., Goldin, T.J., Goto, K., Grajales-Nishimura, J.M., Grieve, R.A.F., Gulick, S.P.S., Johnson, K.R., Kiessling, W., Koeberl, C., Kring, D.A., MacLeod, K.G., Matsui, T., Melosh, J., Montanari, A., Morgan, J.V., Neal, C.R., Nichols, D.J., Norris, R.D., Pierazzo, E., Ravizza, G., Rebolledo-Vieyra, M., Reimold, W.U., Robin, E., Salge, T., Speijer, R.P., Sweet, A.R., Urrutia-Fucugauchi, J., Vajda, V., Whalen, M.T., Willumsen, P.S., 2010. The Chicxulub asteroid impact and mass extinction at the Cretaceous-Paleogene boundary. Science 327 (5970), 1214–1218. https://doi.org/10.1126/science.1177265.

Self, S., Blake, S., Sharma, K., Widdowson, M., Sephton, S., 2008. Sulfur and chlorine in Late Cretaceous Deccan magmas and eruptive gas release. Science 319 (5870), 1654–1657. https://doi.org/10.1126/science.1152830.

Self, S., Schmidt, A., Mather, T.A., 2014. Emplacement characteristics, time scales, and volcanic gas release rates of continental flood basalt eruptions on Earth. Spec. Pap., Geol. Soc. Am. 505. https://doi.org/10.1130/2014.2505(16).

Self, S., Widdowson, M., Thordarson, T., Jay, A.E., 2006. Volatile fluxes during flood basalt eruptions and potential effects on the global environment: a Deccan perspective. Earth Planet. Sci. Lett. 248, 517–531. https://doi.org/10.1016/j.epsl.2006.05.041.

Sial, A.N., Chen, J., Lacerda, L.D., Frei, R., Tewari, V.C., Pandit, M.K., Gaucher, C., Ferreira, V.P., Cirilli, S., Peralta, S., Korte, C., Barbosa, J.A., Pereira, N.S., 2016. Mercury enrichments and Hg isotopes in Cretaceous–Paleogene boundary successions: links to volcanism and palaeoenvironmental impacts. Cretac. Res. 66, 60–81. https://doi.org/10.1016/j.cretres.2016.05.006.

Sinnesael, M., De Vleeschouwer, D., Coccioni, R., Claeys, P., Frontalini, F., Jovane, L., Savian, J.F., Montanari, A., 2016. High-resolution multiproxy cyclostratigraphic analysis of environmental and climatic events across the Cretaceous-Paleogene boundary in the classic pelagic succession of Gubbio (Italy). Spec. Pap., Geol. Soc. Am. 524. https://doi.org/10.1130/2016.2524(09).

Smith-Downey, N.V., Sunderland, E.M., Jacob, D.J., 2010. Anthropogenic impacts on global storage and emissions of mercury from terrestrial soils: insights from a new global model. J. Geophys. Res., Biogeosci. 115. https://doi.org/10.1029/2009JG001124.

Sprain, C.J., Renne, P.R., Clemens, W.A., Wilson, G.P., 2018. Calibration of chron C29r: new high-precision geochronologic and paleomagnetic constraints from the Hell Creek region, Montana. GSA Bull. 130, 1615–1644. https://doi.org/10.1130/B31890.1.

Sprain, C.J., Renne, P.R., Vanderkluysen, L., Pande, K., Self, S., Mittal, T., 2019. The eruptive tempo of Deccan volcanism in relation to the Cretaceous-Paleogene boundary. Science 363 (6429), 866–870. https://doi.org/10.1126/science.aav1446.

Sprain, C.J., Renne, P.R., Wilson, G.P., Clemens, W.A., 2015. High-resolution chronostratigraphy of the terrestrial Cretaceous-Paleogene transition and recovery interval in the Hell Creek region, Montana. Bull. Geol. Soc. Am. 127, 393–409. https://doi.org/10.1130/B31076.1.

Them, T.R., Jagoe, C.H., Caruthers, A.H., Gill, B.C., Grasby, S.E., Gröcke, D.R., Yin, R., Owens, J.D., 2019. Terrestrial sources as the primary delivery mechanism of mercury to the oceans across the Toarcian Oceanic Anoxic Event (Early Jurassic). Earth Planet. Sci. Lett. 507, 62–72. https://doi.org/10.1016/j.epsl.2018.11.029.

Thordarson, T., Self, S., 1996. Sulfur, chlorine and fluorine degassing and atmospheric loading by the Roza eruption, Columbia River Basalt Group, Washington, USA. J. Volcanol. Geotherm. Res. 74, 49–73. https://doi.org/10.1016/S0377-0273(96)00054-6.

Tobin, T.S., Bitz, C.M., Archer, D., 2016. Modeling climatic effects of carbon dioxide emissions from Deccan Traps Volcanic Eruptions around the Cretaceous–Paleogene boundary. Palaeogeogr. Palaeoclimatol. Palaeoecol. https://doi.org/10.1016/j.palaeo.2016.05.028.

Vajda, V., McLoughlin, S., 2004. Fungal proliferation at the Cretaceous-Tertiary boundary. Science 303 (5663), 1489. https://doi.org/10.1126/science.1093807.

Vellekoop, J., Sluijs, A., Smit, J., Schouten, S., Weijers, J.W.H., Sinninghe Damste, J.S., Brinkhuis, H., 2014. Rapid short-term cooling following the Chicxulub impact at the Cretaceous-Paleogene boundary. Proc. Natl. Acad. Sci. 111, 7537–7541. https://doi.org/10.1073/pnas.1319253111.

Vonhof, H.B., Smit, J., 1997. High-resolution late Maastrichtian–early Danian oceanic $^{87}Sr/^{86}Sr$ record: implications for Cretaceous-Tertiary boundary events. Geology 25, 347–350. https://doi.org/10.1130/0091-7613(1997)025<0347:HRLMED>2.3.CO;2.

Witt, M.L.I., Mather, T.A., Pyle, D.M., Aiuppa, A., Bagnato, E., Tsanev, V.I., 2008. Mercury and halogen emissions from Masaya and Telica volcanoes, Nicaragua. J. Geophys. Res., Solid Earth 113. https://doi.org/10.1029/2007JB005401.

Zeebe, R.E., 2012. LOSCAR: Long-term Ocean-atmosphere-Sediment CArbon cycle Reservoir model v2.0.4. Geosci. Model Dev. 5, 149–166. https://doi.org/10.5194/gmd-5-149-2012.